A streamlined workflow for automated cryo focused ion beam milling

Sebastian Tacke[1,4], Philipp Erdmann[2,4], Zhexin Wang[1], Sven Klumpe[2], Michael Grange[1], Jürgen M. Plitzko[2,*], Stefan Raunser[1,*]

[1]Department of Structural Biochemistry, Max Planck Institute of Molecular Physiology, Otto-Hahn-Str. 11, 44227 Dortmund, Germany

[2]Department Molecular Structural Biology, Max Planck Institute of Biochemistry, Am Klopferspitz 18, 82152 Martinsried, Germany

[4]These authors contributed equally

[*]Correspondence: stefan.raunser@mpi-dortmund.mpg.de, plitzko@biochem.mpg.de

Abstract

Cryo-electron tomography is an emerging technique to study the cellular architecture and the structure of proteins at high resolution *in situ*. Most biological specimens are too thick to be directly investigated and are therefore thinned by milling with a focused ion beam under cryogenic conditions. This procedure is prone to frost and amorphous ice depositions which makes it a tedious process, leading to suboptimal results especially when larger batches are milled. Here, we present new hardware that overcomes the current limitations. We developed a new glove box and a high vacuum cryo transfer system and installed a stage heater, a cryo-shield and a cryo-shutter in the FIB milling microscope. This tremendously reduces the ice depositions during transfer and milling, and simplifies the handling of the sample. In addition, we tested a new software application that automates the key milling steps. Together, these improvements allow for high-quality, high-throughput cryo-FIB milling.

Introduction

Electron tomography at cryogenic temperatures (cryo-ET) offers the unique possibility to structurally analyse biological macromolecules in their native cellular environment [Grange2017, Bartesaghi2012]. Using this method, it is even possible to determine protein structures at near-atomic resolution by applying sub-volume averaging techniques [Schur2016].

One prerequisite for electron cryo microscopy (cryo-EM) is that the sample is thinner than the inelastic mean-free-path length of electrons (approximately 350 nm for 300 keV electrons [Vulovic2013]. Thicker samples result in an increased number of inelastically scattered electrons, which decreases the quality of the image. Unfortunately, the majority of biological samples (e.g. eukaryotic cells or tissues) are too thick for cryo-ET and must therefore be thinned.

Cryo-ultramicrotomy is one approach that can be used to reduce specimen thickness. Here, the sample is mechanically cut into ribbons of vitreous sections that are thin enough to be imaged by cryo-ET [Al-Amoudi2004]. However, this method is technically demanding and prone to sample-altering artefacts such as compression, knife marks or crevasses [Al-Amoudi2005]. Another approach uses a focused ion beam under cryogenic conditions (cryo-FIB) in a scanning electron microscope (SEM) to thin samples [Marko2007, Rigort2010]. In recent years, numerous studies have demonstrated the suitability of this technique for preparing biological samples for cryo-ET without the artefacts known from cryo-ultramicrotomy [Hagen2015, Mahamid2016].

Current best-practice protocols for cryo-FIB milling include: i) vitrification of the sample, ii) identification of regions-of-interest (ROI), iii) rough ablation of the surrounding sample material and iv) polishing of the target region, leaving a thin lamella ready for cryo-ET [Schaffer2017]. However, the entire procedure involves multiple handling, transfer, milling and imaging steps. During these steps, samples need to be handled with forceps and it is difficult even for highly experienced practitioners not to destroy the thin and fragile lamellae. Moreover, since the vitrified sample needs to be cooled constantly to avoid a phase transition to hexagonal ice (devitrification temperature around 135 K), it is especially prone to crystalline and amorphous ice contamination. Contamination of polished lamellae is particularly disruptive to cryo-ET as ice crystals often obscure the view on features otherwise visible in the lamellae. It is even possible that ice crystals (frost contamination) conceal the entire lamella,

which prevents any meaningful data acquisition (Figure 1a). Besides the transfer, which bears a high risk of exposing the sample to water, a potential source of (amorphous) ice contamination is the cryo-FIB/SEM itself. Despite the high vacuum inside the SEM, water molecules from the residual gas inside the microscope chamber can still deposit on the sample that is kept well below -140 °C to avoid devitrification. Depending on the partial pressure of water inside the chamber, this effect can be severe and becomes especially problematic when samples reside in the SEM for several hours (Figure 1b,c).

Recently, several software packages that automate the milling process were introduced by ThermoFisher, Zeiss [Zach2020] and the DeMarco group [Buckley2020]. The automation enables the batch milling of up to 20-27 lamellae in 24 h and reduces the time the operator has to spent actively at the SEM. However, during this process the samples remain for many hours in the microscope, which considerably increases contamination and limits the number of lamellae with sufficiently good quality per session.

To obtain optimal lamellae for cryo-ET and to unfold the full strength of automated cryo-FIB milling, the following major hurdles need to be overcome: First, all types of frost contamination need to be reduced to a minimum. Second, all amorphous ice contamination inside the microscope needs to be avoided. Third, the handling of the lamellae must be streamlined to avoid lamella cracking.

Here, we present an integrated workflow that addresses and overcomes all three bottlenecks. In a first step, we implemented a specially designed glove box and a high vacuum cryo transfer system into the current workflow to reduce frost contamination during handling and transfer. Secondly, we tremendously reduced the contamination rates inside the cryo-FIB/SEM by the installation of a stage heater, a cryo-shield and a cryo-shutter. Thirdly, we implemented new tools to simplify the sample preparation and handling.

In addition, we tested the new commercial software application AutoTEM Cryo (ThermoFisher). We show that in combination with this software, the new hardware increases the overall throughput of high-quality lamella production, enabling new types of experiments, which are considered infeasible with current setups.

Results

Sample preparation and handling

After vitrification by plunge or high-pressure freezing, the EM grid with the sample is placed into the Autogrid, then put into the Autogrid shuttle and transferred to the cryo-FIB/SEM. During these steps, the sample needs to be kept at temperatures below -140˚C to avoid devitrification. Consequently, the sample is prone to any kind of contamination. To reduce frost contamination, many cryo-EM laboratories have implemented air-dehumidifier rooms. While those help to reduce the overall humidity, and thereby frost contamination, they cannot completely prevent it.

To reduce frost contamination during handling and simplify implementation of the technique in laboratories unable to control room humidity, we developed a glove box system (Figure 2a) that allows the grid preparation steps to be performed in a tightly regulated atmosphere. During operation, the glove box is constantly purged with dry nitrogen gas (10 ppm H_20) to keep the humidity below the detection limit (1 %) of the humidity sensors used. Beyond functionality, the glove box system was designed to provide maximal convenience during grid preparation. To guarantee that the sample can be brought into the box without disturbing the anhydrous environment inside, we equipped the glove box with a load lock and a port for a high vacuum cryo transfer system. The direct supply of liquid nitrogen is provided by a liquid nitrogen reservoir, which is located inside the glove box. Furthermore, we installed a set of heated tool holders (Figure 2a, marked area) in the box that allow to heat and dry different tools, such as forceps, clipping tools, cassette gripper, etc. directly after usage.

To increase the ease of handling grids inside the box, we designed and built a dedicated universal preparation station (Figure 2b), again maximising the convenience for the user. The station contains an isolated liquid nitrogen bath with three different preparation modules for each step of grid preparation, namely autoloader grid assembly, cryo-FIB shuttle loading and autoloader cassette loading. The users can arrange the needed modules according to their working routine.

To avoid amorphous ice contamination and devitrification during sample transfer from the glove box to the cryo-FIB/SEM, we implemented a previously developed high vacuum cryo transfer system [Tacke2016] (Figure 2c), which consists of a transfer rod, a liquid nitrogen reservoir, a vacuum chamber, a valve and a plug & play adapter for the glove box or cryo-

FIB/SEM. To avoid devitrification during transfer, the cryo-FIB shuttle is actively cooled by the liquid nitrogen reservoir as soon as the transfer rod is retracted in its parking position. Moreover, because the cooled surfaces of the nitrogen reservoir act as a cryo-pump, the vacuum level is kept constant as long as the reservoir is filled [Tacke2016].

With the introduced devices, we are able to minimise the adverse implications, currently associated with existing workflows streamlining the entire grid preparation whilst improving user convenience, efficiency and flexibility. Especially during sample screening, where many samples have to be prepared and transferred over a longer timeframe, the benefit of the devices is apparent. Due to the reduced humidity, the preparation station can stay cooled for several hours without noticeable frost contamination and the high vacuum cryo transfer system allows the necessary quick and contamination-free transfer (Supplementary Video).

Hardware modification of the cryo-FIB

Although cryo-FIB/SEMs are typically operated at high vacuum conditions, contamination of the sample inside the microscope cannot be completely avoided, due to various sources of contamination in the FIB chamber. One of these is the ablated sample material which re-deposits on the specimen. This kind of contamination is greatest at the beginning of lamellae preparation when the sample material is milled in bulk and decreases to a minimum towards the final polishing step. It is therefore not a major problem for the production of lamellae if the milling is performed in two stages: first all sites are roughly milled to a thickness of approximately 500 - 800 nm and only then the final polishing is performed.

The second source of contamination is residual water inside the vacuum chamber. Its deposition/sublimation rate depends on two factors: i) the fraction of water in the residual gas mixture (partial pressure) and ii) the surface temperature of the sample material (Figure 3a). We installed a large cryo-shield and a cryo-shutter to reduce the partial pressure of water in the system to less than 4×10^{-9} mbar and heated the sample to max. -165 ˚C using a newly installed stage heater (Figure 4a, Figure 4b). Combined, these actions moved the ratio between deposition and sublimation closer towards an equilibrium, i.e. minimal deposition rates, which is optimal for cryo-FIB milling (Figure 3a) (see also [Umrath1983], [Echlin1992]).

158 Due to the increased pumping speed, which is the strength of the cryo-pump, the
159 partial pressure decreases from 2-3 x 10^{-7} mbar to approximately 4 x 10^{-9} mbar when the cryo-
160 shield is cooled with liquid nitrogen. After approximately 30 min, the system reaches the
161 lowest partial pressure of water (Figure 3b). If the cryo-shutter is inserted (Figure 4a,b), the
162 partial pressure is reduced even further in the direct vicinity of the sample and under these
163 conditions, the measured contamination rate is (5.6 ± 1.0) nm h^{-1} , (Supplementary Table 1).
164 Although this reduction is already remarkable, we refined the design of the cryo-shutter
165 (Supplementary Figure 1). We minimized the diameter of the ion beam opening (Figure 4c),
166 and completely removed the electron beam opening (Supplementary Figure 1). With the new
167 design, the contamination rate was not measurable anymore (0 ± 2) nm h^{-1} (Supplementary
168 Table 1, Supplementary Figure 2). It should be mentioned, that the initial contamination rate
169 is different for each microscope. Typically, the contamination rate for the used cryo-FIB/SEM
170 is specified to be smaller than 50 nm h^{-1}. In combination, the improved vacuum conditions
171 allow for milling over a longer time course and pave the way for supervised automated milling
172 strategies.
173
174 **Automated lamella production pipeline**
175 The lamella production workflow can be separated in four major steps: i) definition of
176 region(s)-of-interest (ROI), ii) site preparation, iii) rough milling and iv) polishing
177 (Supplementary Figure 3). In this study, we used the software application MAPS (Thermo
178 Fisher Scientific) to visually identify ROIs directly in the cryo-FIB/SEM (Supplementary Figure
179 3a). If it is not possible to visually identify the ROIs or rare biological events, such as for
180 instance cell-cell fusions, are investigated, the correlation of cryo-fluorescent light microscopy
181 and cryo-FIB/SEM should be used. The information of the ROIs is directly transferred to the
182 software application AutoTEM Cryo (Supplementary Figure 3b), where we set the parameters
183 relevant for milling such as ion beam currents, dimensions of the milling pattern, and desired
184 lamellae dimensions. The eucentric height and the milling angle are determined automatically
185 by the program and rough milling, polishing, as well as the milling of micro expansion joints
186 (relief cuts) to release the stress of the support layer [Wolff2019] are then executed in a fully
187 automated manner (Supplementary Figure 3b, 4). This process resulted in up to 27 lamellae
188 per session (16 h) with a final thickness of 100 - 200 nm (Supplementary Figure 3d).
189

190 **Efficiency estimation and quality assessment**

191 To estimate the efficiency of our lamellae preparation pipeline, that is the production
192 of thin and intact lamellae, we separated the handling steps into two parts: i) the pre-
193 processing and ii) the post-processing. The pre-processing includes the assembly of the
194 autoloader grid, its loading to the cryo-FIB shuttle and the transfer of the shuttle from the
195 glove box to the cryo-FIB. The post-processing step comprises the transport from the cryo-
196 FIB/SEM to the glove box and the transfer of the autoloader grid from the cryo-FIB shuttle to
197 the autoloader cassette.

198 In recently published preparation protocols, the success rate of obtaining suitable
199 specimens for proficient users was estimated to be 80% for the pre-processing and 90% for
200 the post-processing step, which results in a total efficiency of 72% [Medeiros2018]. In reality,
201 the efficiency is much lower because some lamellae are usable for cryo-ET analysis.

202 Our improvements of the pre- and post-processing steps resulted in a considerably
203 higher efficiency exceeding 96% throughout the entire process (pre- and post-processing).
204 During pre-processing no grid was lost and only 7 out of the 198 lamellae cracked during the
205 post-processing. In addition, all intact lamellae were almost contamination free (Figure 5a).
206 Applying the improved hardware, on average, only 9% of the lamella areas were covered with
207 ice particles (Figure 5b) compared to 20% using the standard set up (Figure 5b, Figure 1a, Table
208 1). Importantly, in line with the fact that contamination inside the cryo-FIB/SEM was below
209 the detection limit, we could not identify any contamination layer in the final tomograms
210 (Figure 5c) and approximately 90% of all intact lamellae were useable for cryo-ET
211 investigations (Table 1). Taken together, the high efficiency and tremendously reduced
212 contamination rate reflect the impact of the newly implemented hardware components.

213 To assess the quality of the automated lamellae preparation, we applied the
214 automated lamella production pipeline as described above. We investigated different types
215 of specimens and quantified the success rates for the rough milling and polishing. We
216 considered a milling task as successfully completed, if the following criteria were fulfilled: i)
217 the lamella was intact, i.e. not broken, ii) the desired thickness was reached, iii) tracking of the
218 lamella site was successful, i.e. the right position of the sample was milled. We determined an
219 average success rate of 96% and 88% for the rough milling and polishing, respectively (Table
220 2). With the estimated efficiency of 96% for the pre- and post-processing and the calculated
221 efficiency of 84% for the milling process, the efficiency of the total workflow can be estimated

222 to be around 80%. Although the success rate was much higher in the case of manual milling
223 (above 95%), the total throughput is much higher, and could be further increased with
224 overnight runs. Moreover, the operator time is significantly reduced.

225 To demonstrate that lamellae, prepared by automated cryo-FIB milling using AutoTEM
226 cryo, are suitable for subtomogram averaging, a set of ribosomes were identified on several
227 lamellae (Figure 6a,b). With only 15,000 particles, a structure of 14 Å (0.143 FSC criteria) was
228 calculated (Figure 6c, e). Since the orientations and locations can be precisely determined, we
229 were able to identify polysomes (Figure 6d).

230 Taken together, these results clearly demonstrate that the streamlined workflow not
231 only increases the overall throughput of the lamellae production but also generates results
232 that are suitable for in-situ high-resolution investigations.

233

234 Discussion

235 Contamination of the samples and inconvenient sample handling are the dominant
236 bottlenecks of current cryo-FIB workflows, which can decrease the quality of the final lamellae
237 and limit the overall throughput per milling session. In the present study we overcame the
238 aforementioned limitations by the introduction of new hardware components (Table 3) and
239 show that the new hardware in combination with automatic cryo-FIB milling increases the
240 overall throughput of high-quality lamella production.

241 To reduce frost contamination throughout the entire preparation process, we
242 introduced a glove box and a high vacuum cryo transfer system. Moreover, we reduced the
243 amorphous ice contamination rates inside the vacuum system to a non-measurable level,
244 mainly because of the installation of an additional cryo-shield and a cryo-shutter. Now, the
245 entire handling and transfer steps as well as the cryo-FIB milling can be performed in an almost
246 anhydrous environment. In order to streamline the handling of the grids carrying fragile
247 lamellae, we introduced a new preparation station, which aims at avoiding all types of adverse
248 environmental implications related to sample handling with maximal convenience for the
249 user.

250 The contamination rate of 50 nm h^{-1} in the initial cryo-FIB/SEM setup limited the total
251 number of prepared lamellae per session. Due to the improved and new hardware, we could
252 prevent contamination in the milling position. Therefore, the lamella production is not

253 restricted to a specific time frame anymore and, if a suitable automated filling system is in
254 place, an 24/7 operation is even possible now.

255 We tested the new software application AutoTEM Cryo, which successively processes
256 a queue of lamella sites in a supervised to automated manner, allowing for automatic batch
257 milling of many lamellae. With the help of AutoTEM Cryo, the time spent on the microscope
258 is now reduced to approximately 5 minutes per lamella site at the beginning of the milling
259 process. Because of the automation of Aquilos cryo-FIB milling, we can now fully exploit the
260 benefits of the hardware improvements and can indeed prepare up to 27 lamellae per session.
261 All lamellae preparations in the present study were performed in sessions with an operation
262 time of 8-16 hours.

263 In addition, the supervised automated milling process allows users to explore the
264 influence of different milling parameters and strategies in a systematic manner. Due to the
265 higher throughput, quality assessment routines can be developed and once these routines are
266 established, the influence of different milling parameters can more readily be investigated,
267 for example the influence of high ion currents (2-3 nA) on the quality of the cryo-lamella,
268 which is not yet fully understood.

269 Without the contamination layer the tracking of the ROI position can be more easily
270 determined by the AutoTEM Cryo software application. This became especially apparent in
271 the case of myofibrils that due to their limited width proved to be a challenging sample for
272 cryo-FIB milling. The improved conditions in the FIB-SEM tremendously increased the success
273 rate of obtaining useable lamellae from ~ 65% to ~ 85% (Table 1).

274 Taken together, the combination of new hard- and software increases the overall
275 throughput of lamellae production, improves the quality of the lamellae, and simplifies the
276 process of cryo-FIB milling and sample transfer. In addition, the hardware components
277 described in this work enable new types of experiments, which were previously difficult to
278 realize.

279

280 Data availability

281 The major hardware components developed in this study, such as the glove box, preparation
282 station, and cryo shutter (Type II) can be purchased at Delmic B.V.

283

284 Acknowledgements

We thank Sagar Khavnekar and Florian Beck for help with subtomogram averaging. This work was supported by funding from the Max Planck Society (to S.R. and J.P.). M.G. is supported by an EMBO Long-Term Fellowship.

Material and Methods

Glove box, preparation station and high vacuum cryo transfer

The glove box has been manufactured by Microscopy Solutions Py. Ltd and modified by us accordingly. Before sample preparation, the glove box was purged overnight with dry nitrogen (10 ppm H_2O). Before the sample was brought into the glove box through the load lock, the liquid nitrogen reservoir and the preparation station were filled with liquid nitrogen. Then, EM grids were clipped to the autogrids, if not already done. Thereafter, the Autogrids were loaded into the cryo-FIB shuttle and transferred to the cryo-FIB/SEM (Aquilos, Thermo Fisher Scientific) via the high vacuum cryo transfer system. After the milling session was started, both the glove box as well as the preparation station were baked out at 40-50 °C with the help of the installed heaters. After milling, the cryo-FIB shuttle with the sample was transferred back to the glove box and the autoloader grids were unloaded, rotated by 90° and mounted to the autoloader cassette. Finally, the cassette was loaded into the NanoCab (Thermo Fisher Scientific) and transferred to the electron cryo microscope (Titan Krios, Thermo Fisher Scientific).

305 **Cryo-FIB/SEM**

306 The developments described in this study were carried out on an Aquilos cryo-FIB/SEM
307 (Thermo Fisher Scientific), equipped with a larger cryo-shield (manufactured by CryoVac
308 GmbH & Co KG), a cryo-shutter (in-house production) and stage heater (in-house production).
309 The instrument was equipped with a gas injection system (GIS) and a platinum sputter coater
310 (Thermo Fisher Scientific). After insertion, the grids were coated with an organometallic
311 platinum layer to protect the sample while milling. The sputter coating was utilized to avoid
312 charging effects during imaging in the SEM and can either be done before and/or after GIS
313 deposition. For scanning electron imaging, an acceleration voltage of 2-5 kV with an electron
314 current of max. 28 pA was used. The ion optics were operated at 30 kV acceleration voltage
315 with different ion currents (50 – 700 pA). All ion currents were specified by the user and should
316 be tuned for every new sample material. The alignment of the ion optics is crucial and was
317 performed at least once a week to avoid massive image shifts while changing the ion currents.
318 For scanning electron imaging, the installed Everhart-Thornley detector was utilized.

319

320 **Automated milling via AutoTEM Cryo**

321 Although the relevant milling parameter as ion beam currents, milling patterns and milling
322 time might vary for different types of sample, a brief overview is given:

323 After the visual identification of ROIs via the software application MAPS (Thermo Fisher
324 Scientific), the lamella sites were imported to the software application AutoTEM Cryo (Thermo
325 Fisher Scientific). Thereafter, the automated milling routine was started. During the first step
326 (preparation), the eucentric height and the milling angle were determined automatically.
327 During the final action of the preparation step, the user was able to adjust the final milling
328 position. In total, the preparation step takes approximately 2-3 min for each lamella site.
329 Thereafter, relevant milling parameters were defined or loaded from a former template. The
330 lamella width is mostly defined by the type of sample material and the condition of the specific
331 ROI. Lamella widths of 8 – 10 µm were typically used. The desired lamella thickness was
332 project dependent: in some cases, the project required a lamella thickness below 150 nm and
333 in other cases, a thickness of 250 nm was still within the required limits. For the first estimation
334 of milling times, a total sample thickness of 15 µm was assumed.

335 In the first milling step, the chunk milling, relief cuts were milled to release the stress
336 from the support film of the grid, which might occur during plunge freezing. Here, a width of

337 1-3 µm and a height of 10-15 µm were typically used. The relief cuts were milled at relatively
338 high ion beam currents (0.5–1 nA) for approximately 3-5 min.
339 Thereafter, most of the bulk material was removed during rough milling. This task is
340 separated into four different milling steps. During the first milling step, most of the sample
341 material was ablated with relatively high ion beam currents (0.5–1 nA) until a lamella thickness
342 of approximately 2-3 µm was reached. In the following milling steps, the ion currents were
343 consecutively reduced from 0.5 to 0.1 nA. After these milling steps, the lamellae thickness was
344 already reduced to 300-600 nm. For the initial rough milling the front and rear pattern height
345 were set to 5-7 µm. All later milling pattern were calculated accordingly. Since most of the
346 sample material was removed during rough milling, most of the time was spent during this
347 step (20-30min).
348 The polishing step was executed in three successive milling steps with an ion beam
349 current of 30-50 pA. Since most of the sample material was already ablated, the last polishing
350 process took only approximately 10 - 15 min.
351
352 **Cryo-electron tomography and tomogram reconstruction**
353 All data sets were collected on a Titan Krios (Thermo Fisher), operated at an acceleration
354 voltage of 300kV. The microscope was equipped with a field emission gun, a BioQuantum
355 imaging filter (Gatan, Munich, Germany) with a set energy width of 20eV and a K3 direct
356 electron detector (Gatan, Munich, Germany). The software package SerialEM was used for
357 automated data acquisition [Mastronade2005]. For reconstruction of the tomograms, the
358 software package IMOD was used [Kremer1996]. Imaging conditions are listed in
359 Supplementary Table 2.
360
361 **Template Matching, Polysome Detection and Visualization**
362 Tomograms were binned (IMOD bin 8x, 14.32 Å pix^{-1}) and template matching was performed
363 using PyTom [Hrabe2012]. First, a reference was constructed from approximately 300
364 manually picked ribosomes, which were aligned in PyTom using the fast-rotational matching
365 (FRM) algorithm. The reference obtained from this was then truncated at the small subunit to
366 allow later removal of false positives. For each tomogram, the 800 highest-scoring cross-
367 correlation peaks were extracted, and the subtomograms aligned and classified using a
368 maximum likelihood approach in Relion 3 [Zivanov2018] to remove false positives. This was
369 judged by the absent small subunit in the false positive class averages. After initial processing

370 at bin 8x, further classification and refinement of the 2x binned (3.58 Å pix^{-1}) subtomogram
371 averages was performed in Relion, including normalization and CTF estimation with CTFFIND
372 4.1.5 [Rohou2015]. The final list of particles (approximately 15000) yielded a ribosome
373 structure at 14 Å resolution (0.143 FSC criterion), which was used in all animations. Polysome
374 detection was performed analogously to published using an inhouse Matlab script
375 [Brandt2010].

376 **Frost Contamination Measurements**

377 To quantify the reduction of frost contamination, three lamellae preparations were performed
378 with the standard configuration of the cryo-FIB/SEM and three preparations with the
379 developed hardware upgrades (glove box, preparation station and high vacuum cryo transfer).
380 After milling, overview images (montages) of each lamella were taken with the TEM. Each
381 overview was analysed regarding the frost contamination by outlining each contamination
382 spot manually (Figure 1a, Figure 5a). Only contaminations in direct contact with the lamella
383 were taken into account. To avoid user bias, any contamination, regardless of its impact on
384 the final data acquisition, was used for the analysis. Finally, the ratio of contaminated area
385 and total lamella area was calculated (Figure 5b). The total lamellae area and the
386 contaminated area were summed and the ratio was calculated for both conditions. For both
387 conditions, a total area of approximate 3000 μm^2 were analysed (Table 1). Whereas the
388 experiments with the standard configuration were performed with a room humidity of
389 approximately 30%, the experiments with the hardware upgrades were performed with a
390 room humidity of 50-60%.

391 **Amorphous Ice Contamination Measurements**

392 To quantify the impact of the hardware, which was installed inside the cryo-FIB/SEM (cryo-
393 shield, cryo-shutter and stage heater), the growth of the amorphous ice contamination was
394 measured. One day before the measurement, plain grids (Quantifoil 2/2) were transferred to
395 the microscope. Directly before the measurement, the stage was moved into the milling
396 position and thereafter, the cryo-FIB/SEM was cooled. One hour after cooling, the baseline
397 images were taken. The next image was taken after at least two hours. For imaging, the sample
398 stage was rotated by 110° and tilted by 30°. The following imaging conditions were used for
399 all measurements: Acceleration voltage: 5 kV, working distance: 7mm, electron current: 25
400 pA, exposure time: 1 µs, pixel size: 1 nm, detector: T2 A+B, imaging mode: *optitilt*. For each

measurement, two to three positions in different areas of the grid, including at least four holes each, were utilized. For every hole, the baseline thickness and the thickness with the gained contamination were determined (Supplementary Figure 2) and corrected for its residual tilting angle. Finally, all measurements of the specific condition were averaged.

Figures

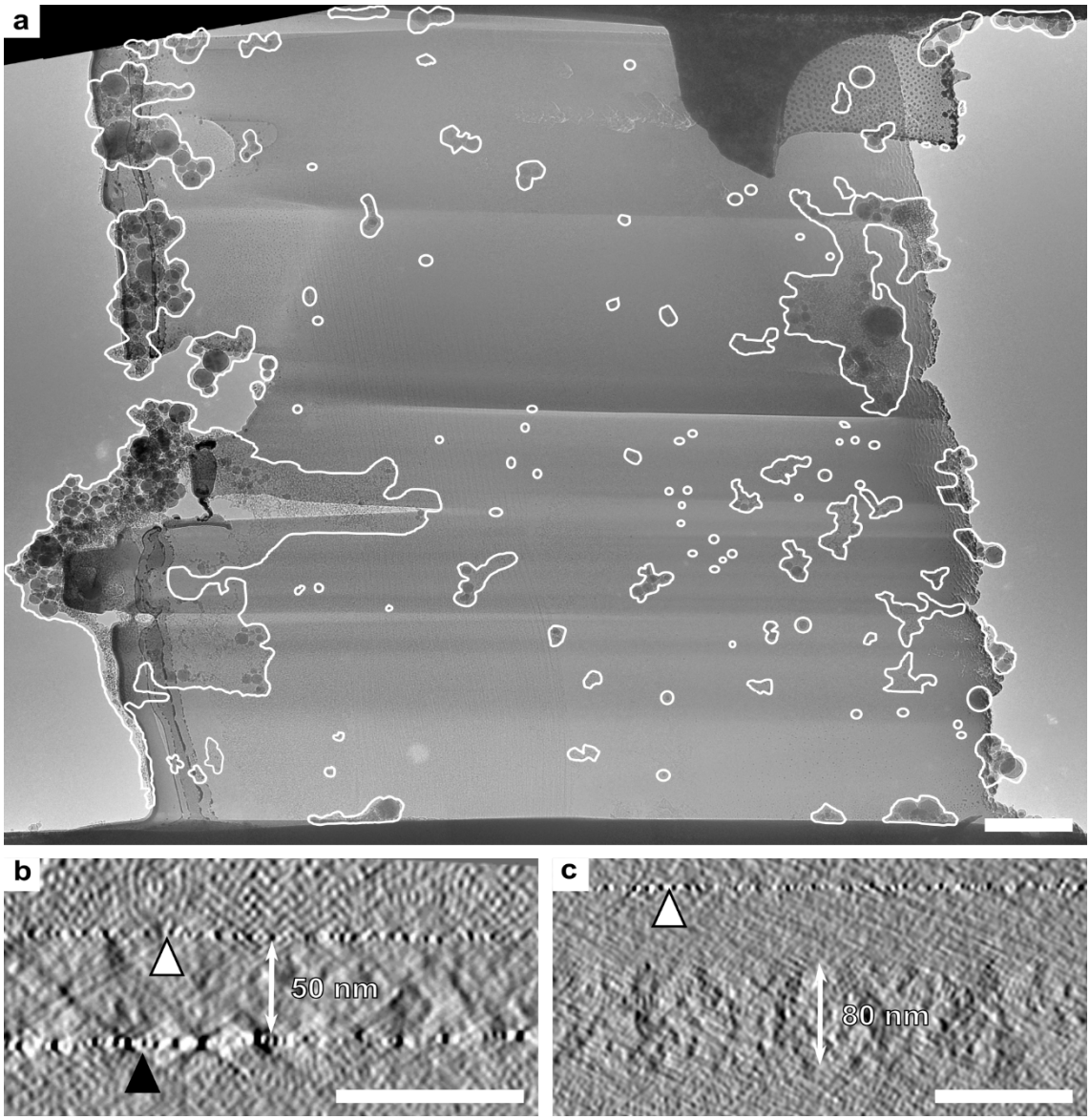

Figure 1: Possible artefacts arising during handling, transfer and processing. a) Overview of a lamella, which was prepared under standard conditions without hardware upgrades. When the sample transferred in a hydrous environment, ice crystals of different sizes (highlighted by marked areas) contaminate up to 20% of the lamella area. Scale bar, 1 µm. **b,c**) Side views of two tomograms, taken from two different lamellae, prepared in the same milling session. The lamella in (**b**) was polished last. Thus, it was taken out of the SEM almost directly after polishing. Consequently, the water deposition is not detectable. The sputter layer (white triangle) is directly on top of the lamella. The black triangle marks some platinum re-deposition. The lamella in (**c**) was polished approximately 1 hour before the lamella in (**b**) and stayed the whole time in the SEM. In this case, a ~50 nm thick water deposition can be identified on top of the 80 nm thick lamella, reducing its quality. The platinum coating above the sample material is indicated by a white triangle. Scale bars, 100 nm.

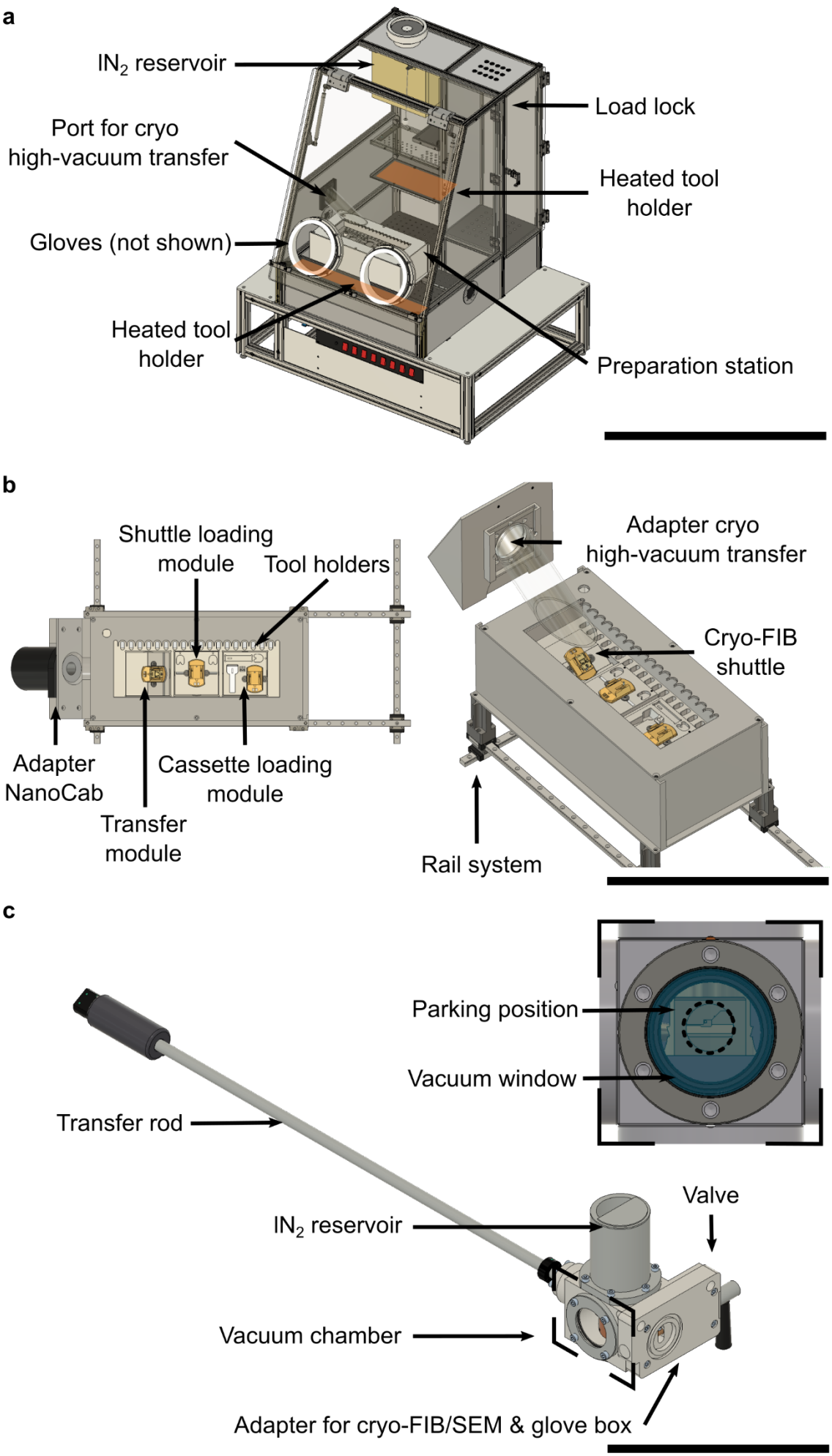
a
IN2 reservoir
Port for cryo
high-vacuum transfer
Gloves (not shown)
Heated tool
holder
Load lock
Heated tool
holder
Preparation station
b
Shuttle loading
module
Tool holders
Adapter
NanoCab
Transfer
module
Cassette loading
module
Adapter cryo
high-vacuum transfer
Cryo-FIB
shuttle
Rail system
c
Parking position
Vacuum window
Transfer rod
Valve
IN2 reservoir
Vacuum chamber
Adapter for cryo-FIB/SEM & glove box

419

Figure 2: Schematic of the glove box, the preparation station, and the high vacuum cryo transfer system. a) The glove box enables convenient sample handling in an anhydrous environment. To reduce the humidity to a minimum, the glove box is purged during operation with nitrogen and a cold trap is installed in the back of the lN_2 reservoir. lN_2 can be taken from this reservoir for applications inside the glove box. For convenient handling, heated tool holders are installed. A load lock enables the insertion of tools without breaking the humidity barrier. Scale bar, 600 mm. **b**) A new preparation station guarantees a comfortable and secure handling of the sample material. The preparation station consists of four parts: the liquid nitrogen bath, the preparation modules, the adapter for the transfer systems and the adapter for the NanoCab. All modules can be re-arranged inside the liquid nitrogen bath according to the preferences of the operator and are designed for left- and right-handed persons. Clipped autoloader C-clip rings can be loaded onto the cryo-FIB shuttle or to the autoloader cassette using the corresponding modules. Also clipping is possible in the preparation station but is not shown in this overview. The preparation station is mounted onto a rail system to ensure highest flexibility inside the glove box. Scale bar, 400 mm. **c**) The high vacuum cryo transfer system consists of a transfer rod for picking up the cryo-FIB shuttle, a vacuum chamber, liquid nitrogen reservoir, a valve and the adapter for the cryo-FIB/SEM and glove box. The sample can be picked up by the transfer rod and is inserted in the vacuum chamber. Inside the vacuum chamber the cryo-FIB shuttle is placed in a parking position. Here, the shuttle is actively cooled by the lN_2 reservoir. The liquid nitrogen acts also as a cryo-pump and maintains the vacuum level, while the high vacuum cryo transfer is disconnected from the pumps. The lN_2 volume holds for approximately 30 min. After the shuttle is positioned in the parking position, the valve towards the glove box is closed and the high vacuum cryo transfer is evacuated. Thereafter, the valve at the transfer system is closed and the sample can be transferred to the cryo-FIB/SEM. Scale bar, 300 mm.

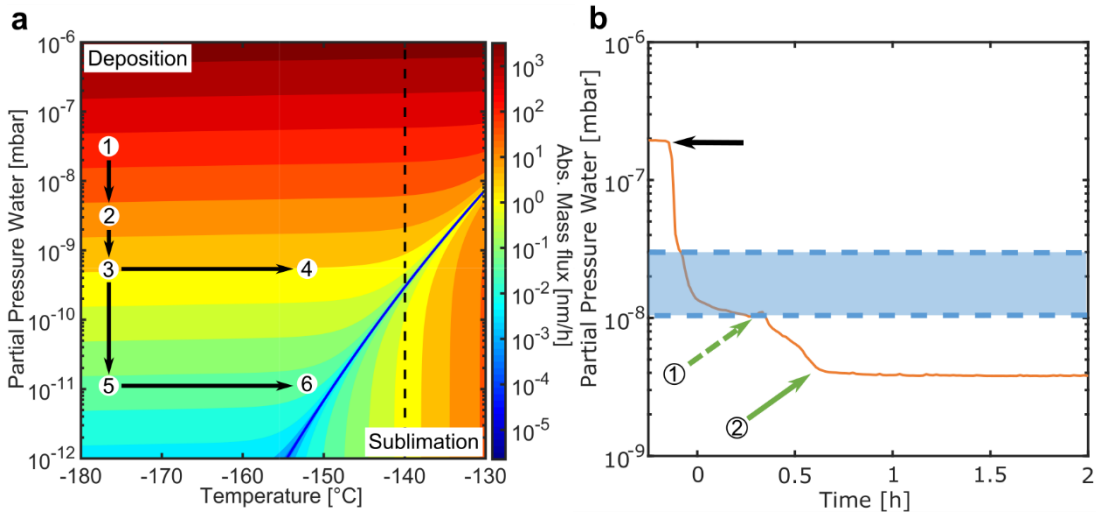

Figure 3: Phase diagram of water. a) Phase diagram of water and the associated mass flux (deposition/sublimation) [Umrath1983]. The encircled numbers mark the different measurement conditions. The dashed line indicates the devitrification temperature of water. The arrows indicate our strategy to minimize the ice deposition (amorphous ice contamination) onto the sample. After the installation of the cryo-shield, cryo-shutter Type I and stage heater, the contamination rate increases from the specified 50 nm h^{-1} to 85 ± 7 nm h^{-1} (condition 1). As soon as the cryo-shield is cooled, the partial pressure of water drops to 4 x 10^{-9} mbar and the contamination rate decreases to 72 ± 4 nm h^{-1} (condition 2). When the cryo-shutter Type I is inserted, the partial pressure in the vicinity of the sample decreases by approximately one order of magnitude (condition 3), which reduces the contamination rate to 12.8 ± 1.6 nm h^{-1}. To reduce the contamination rate even further, the sample is heated to approximately -165 °C. Since there might be a temperature difference of 15 °C between the stage and the shuttle, the temperatures for condition 4 and 5 are specified as approximately -150 °C. The heating reduces the contamination rate to 5.6 ± 1.0 nm h^{-1} (condition 4), which is already a tremendous improvement compared to the initial contamination rate of 50 nm h^{-1}. To reduce the contamination even further we designed the more effective cryo-shutter Type II (Supplementary Figure 1). Using this shutter, we were able to reduce the contamination to a non-detectable level (-0.6 ± 1.3 nm h^{-1}) (condition 6), even without heating the sample (0 ± 2 nm h^{-1}) (condition 5). **b**) Measured partial pressure of water inside the cryo-FIB/SEM chamber (orange graph). As soon as the SEM and cryo-shield are cooled (black arrow), water molecules from the residual gas get trapped and the partial pressure decreases. After 15 min, the stage reaches its end temperature of -185°C (dashed green arrow). Under this condition, the impact of the cryo-shield is still neglectable, since its temperature is still above -100°C. After 30 min, also the cryo-shield reaches its end temperature and the system reaches its final partial pressure value (solid green arrow). The blue area indicates the partial pressure regime of standard cryo-FIB/SEM instruments.

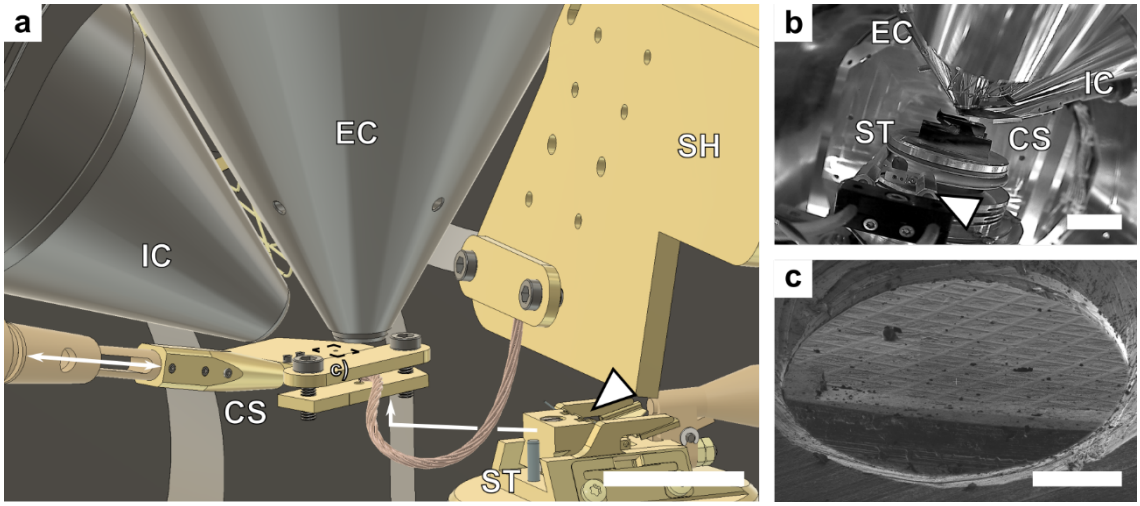

Figure 4: Cryo-shield and cryo-shutter. **a**) Schematic of the cryo-FIB/SEM chamber. The installed cryo-shield (SH) is installed next to the electron column (EC) and the ion column (IC). The total surface area of the cryo-shield (SH) is approximately 880 cm^2. Assuming that the strength of the pump is ~ 15 l cm^{-2} s^{-1} [Bello2017], the estimated total pumping speed is ~ 13,000 l s^{-1}. To reduce the partial pressure in the vicinity of the sample even further, a cryo-shutter (CS) can be inserted during milling (white arrow). The shuttle with the autoloader grids (white triangle) is moved via the cryo stage (ST) right below the cryo-shutter. Two different cryo-shutter types were tested (Supplementary Figure 1). Cryo-shutter Type II covers most of the grid reducing the contamination rate even further compared to the cryo-shutter Type I. Scale bar, 25 mm. **b**) Camera image from the back of the chamber. The cryo-shutter covers the autoloader grids almost completely. The white triangle indicates the position of the stage heater (not installed in this image). Scale bar, 25 mm. **c**) Ion image of the cryo-shutter Type II, showing the EM grid through the shutter hole. The diameter of the shutter hole is approximately 1 mm to ensure a complete protection of the grid. For electron imaging, the shutter is removed automatically. With these improvements, the sample can be prepared and stored in the milling position until imaging without amorphous ice contamination. Scale bar, 300 µm.

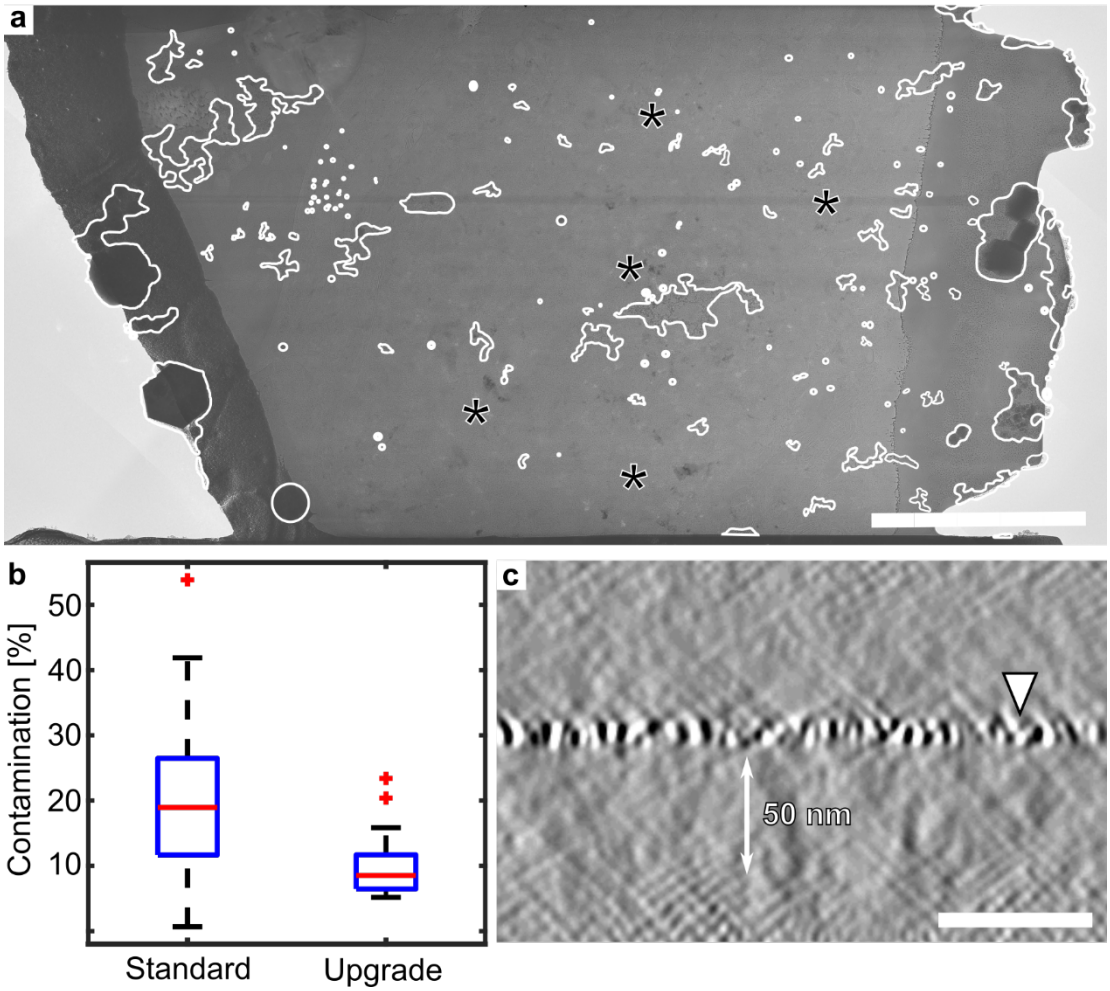

Figure 5: Quality assessment of the pre- and post-processing step. **a**) Overview of a lamella prepared with all hardware upgrades in use. In this case, only 8% of the lamella surface were covered with frost contamination. Most of the ice crystals are small enough that data acquisition is still possible. In some areas, non-vitrified regions can be identified (asterisks). Scale bar: 5 µm. **b**) Boxplot diagram of the frost contamination analysis. We analyzed 3000 μm^2 of lamellae produced before and after our hardware upgrades revealing that the average frost contamination was on average reduced from 20% to 9% after installation of the new components. **c**) Side view of a lamella, prepared with all hardware upgrades in use. As indicated (white triangle), the sputter layer is directly on top of the lamella, indicating that no contamination occurred during milling. Scale bar: 50 nm.

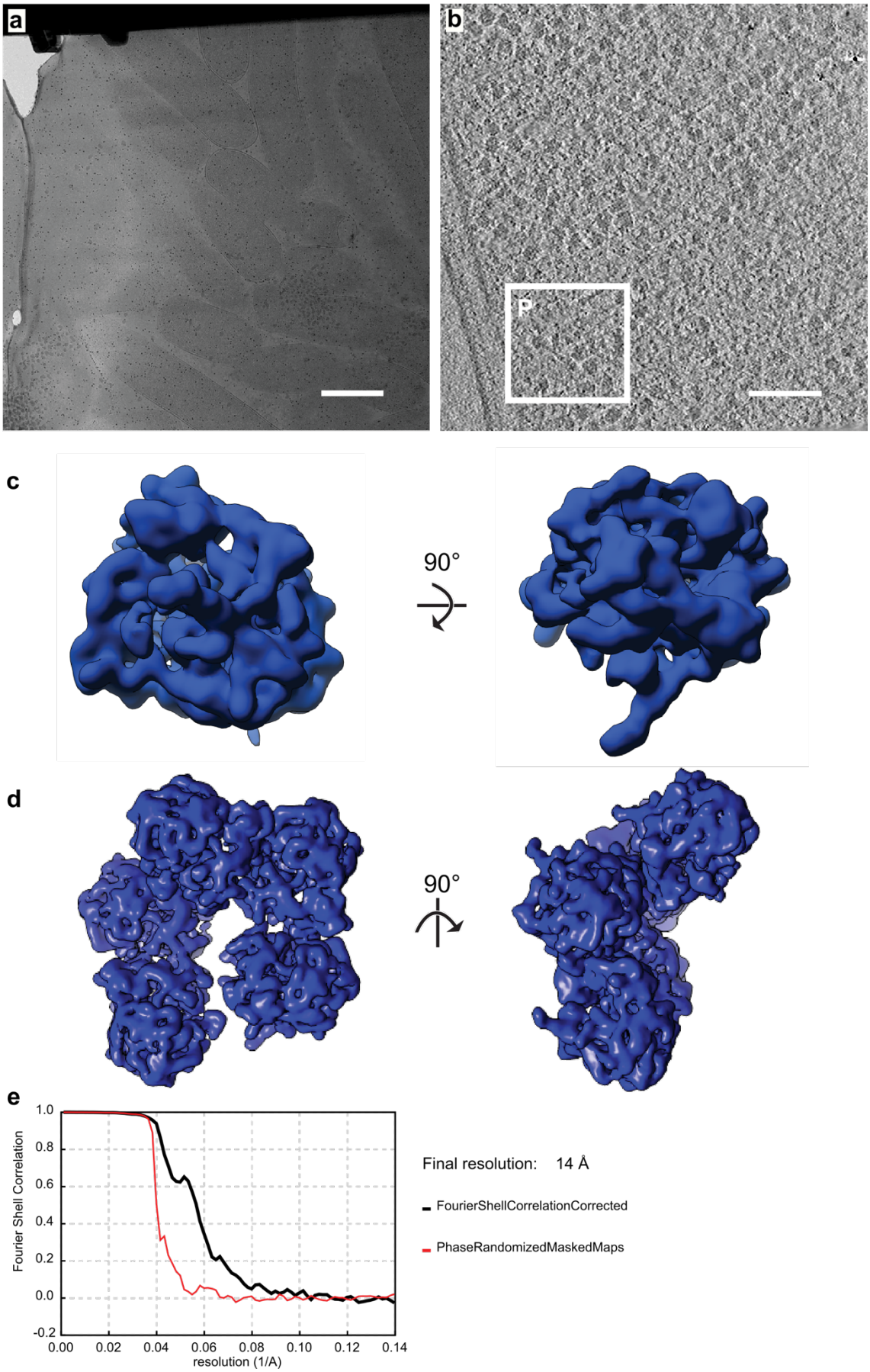

Figure 6: Suitability of automatically milled lamellae for subtomogram averaging. a) Representative overview of an automatically milled lamella (*E. coli*). The lamella was sputter

506 coated to reduce charging artefacts. Scale bar, 2.5 µm. **b**) Macromolecular complexes such as
507 ribosomes are readily detectable. Scale bar, 100 nm. **c**) Subtomograms can be averaged to
508 high resolution (14 Å at 0.143 FSC criterion). **d**) Additionally, orientations and locations can be
509 precisely determined, which enabled the detection of polysomes up to a pentamer (insert and
510 boxed region P in (**a**)). **e**) FSC-curve of the final ribosome reconstruction.

511

Experiment (sample)	Hardware upgrades	Number of ROIs	Successfully milled lamellae	Max. contamination thickness [nm]	Average area covered by ice crystals
Myofibrils	no	18	12	50	
Myofibrils	no	11	6	100	20 %
Cardiomyocytes	no	11	8	n.a.	
Success rate			**65 %**		
Myofibrils	yes	11	11	0	
Myofibrils	yes	16	14	0	9 %
Cardiomyocytes	yes	7	4	0	
Success rate			**85%**		

512

513 **Table 1: Impact of the hardware modifications on the frost contamination.** To determine the
514 impact of the hardware upgrades, the frost contamination without and with hardware
515 upgrades was determined (Figure 5b). For each condition, three milling session were
516 performed. An overview of each lamella was taken and the frost contamination was
517 determined manually. Finally, the contaminated and total area were summed and the ratio
518 was calculated.

519

520

Sample	Number of ROI (lamellae sites)	Number of successfully roughly milled lamellae	Number of successfully polished lamellae
Myofibrils	56	53	43
Cardiomyocytes	18	18	12
A9 cells	7	6	6
S. cerevisiae	94	89	85
E. coli	23	23	21
Neurons	3	3	2
HeLa cells	6	6	6
Sum	207	198	175
Success rate		**96%**	**88% (total 84%)**

521

522 **Table 2: Milling statistics for different types of sample material using the automated**

523 **lamella production pipeline.**

524

525

Step in workflow	Possible contamination	Implication	Current technology/ limitations	New technology/ improvements
Sample Vitrification	Ice particles	Lack of visibility of sample surface	Air-dehumidified rooms	Not addressed
Cryo-FIB/SEM Loading	Ice particles and condensation	Lack of visibility and curtaining	Aquilos loading station: No regulated environment Limited runtime (~ 1 h)	Glove Box, preparation station, high vacuum cryo transfer: Anhydrous environment Extended runtime (> 3 h)
Cryo-FIB/SEM Milling	Condensation	Increased thickness of lamella	Cryo-shielding: Contamination rate ~ 50 nm h^{-1} Limit of throughput	Extra shielding, cryo-shutter, stage heater: No contamination High throughput
Cryo-FIB/SEM Unloading	Ice particles and condensation	Increased thickness of lamella	Aquilos loading station: No regulated environment Limited runtime (~ 1 h) Cassette loading not possible	Glove Box, preparation station, high vacuum cryo transfer: Anhydrous environment Extended runtime (> 3 h) Cassette loading possible
Sample Storage	Ice particles	Loss of viewable areas	Grid box and Dewar	Not addressed

526 **Table 3: Overview of the improvements of the cryo-FIB/SEM workflow**

527

528 **References**

529

530 [Grange2017] Grange, M, Vasishtan, D., & Grünewald, K. Cellular electron cryo tomography
531 and in situ sub-volume averaging reveal the context of microtubule-based processes. *J. Struct.*
532 *Biol.* **197**, 181-190 (2017).

533

534 [Bartesaghi2012] Bartesaghi A. et al. Secondary Structure Determination by Constrained
535 Single-Particle Cryo-Electron Tomography. *Structure* **20**, 2003-2013 (2012).

536

537 [Schur2016] Schur, F. K. M. et al. An atomic model of HIV-1 capsid-SP1 reveals structures
538 regulating assembly and maturation. *Science* **353**, 506-508 (2016).

539

540 [Vulovic2013] Vulovic, M. et al. Image formation modelling in cryo-electron microscopy. *J.*
541 *Struct. Biol.* **183**, 19-32 (2013).

542

543 [Al-Amoudi2004] Al-Alamoudi, A., Norlen, L.P.O., & Dubochet J. Cryo-electron microscopy of
544 vitreous sections of native biological cells and tissues. *J. Struct. Biol.* **148**, 131-135 (2004)

545

546 [Al-Amoudi2005] Al-Alamoudi, A., Studer, D. & Dubochet, J. Cutting artefacts and cutting
547 process in vitreous sections for cryo-electron microscopy. *J. Struct. Biol.* **150**, 109-121 (2005).

548

549 [Marko2007] Marko, M. et al. Focused-ion-beam thinning of frozen-hydrated biological
550 specimens for cryo-electron microscopy. *Nat. Methods* **4**, 215-217 (2007).

551

552 [Rigort2010] Rigort, A. et al. Micromachining tools and correlative approaches for cellular
553 cryo-electron tomography. *J. Struct. Biol.* **172**, 169-179 (2010).

554

555 [Hagen2015] Hagen C. et al. Structural basis of vesicle formation at the inner nuclear
556 membrane. *Cell* **163** 1692-1701 (2015).

557

558 [Mahamid2016] Mahamid J. et al Visualizing the molecular sociology at the HeLa cell nuclear
559 periphery. *Science* **351**, 969–972 (2016).

[Schaffer2017] Schaffer, M. et al. Optimized cryo-focused ion beam sample preparation aimed at in situ structural studies of membrane proteins. *J. Struct. Biol.* **197**, 73-82 (2017).

[Medeiros2018] Medeiros, J.M. et al. Robust workflow and instrumentation for cryo-focused ion beam milling of samples for electron cryotomography. *Ultramicroscopy* **190**, 1-11 (2018).

[Zach2020] Zach, T. et al. Fully automated, sequential focused ion beam milling for cryo-electron tomography. *Elife* **9,** e52286 (2020).

[Buckley2020] Buckley, G et al. Automated cryo-lamella preparation for high-throughput in-situ structural biology. *Journal of Structural Biology* **210**, 107488 (2020).

[Tacke016] Tacke, S. et al. A Versatile High-Vacuum Cryo-transfer System for Cryo-microscopy and Analytics. *Biophysical Journal* **110** 4, 758-765 (2016).

[Echlin1992] Echling, P. Low-Temperature Microscopy and Analysis. Plenum Publishing Corporation, New York (1992)

[Umrath1983] Umrath, W.W. Berechnung von Gefriertrocknungszeiten für die elektronenmikroskopische Präparation. *Mikroskopie* **40**, 9-34 (1983).

[Wolff2019] Wolff, G. Mind the gap: Micro-expansion joints drastically decrease the bending of FIB-milled cryo-lamellae. *J. Struct. Biol*. In Press (2019).

[Mastronade2005] Mastronarde D.N. Automated electron microscope tomography using robust prediction of specimen movements. *J. Struct. Biol.* 152, 36–51 (2005).

[Hrabe2012] Hrabe, T. et al. PyTom: a python-based toolbox for localization of macromolecules in cryo-electron tomograms and subtomogram analysis. *J. Struct. Biol.* **178**, 177-188 (2012).

592 [Zivanov2018] Zivanov, J. et al. New tools for automated high-resolution cryo-EM structure
593 determination in RELION-3. *eLife* **7**, e42166 (2018).
594
595 [Rohou2015] Rohou, A. and N. Grigorieff, CTFFIND4: Fast and accurate defocus estimation
596 from electron micrographs. *J. Struct. Biol.* **192**, 216-221 (2015).
597
598 [Brandt2010] Brandt, F. et al. The Three-Dimensional Organization of Polyribosomes in Intact
599 Human Cells. *Mol. Cell* **39**, 560-569 (2010).
600
601 [Kremer1996] Kremer, J.R., Mastronarde, D.N. & McIntosh, J.R. Computer visualization of
602 three-dimensional image data using IMOD. *J. Struct. Biol.* **116**, 1-6 (1996).
603
604 [Bello2017] Bello, I. Vacuum and Ultravacuum: Physics and Technology. CRC Press (2017)
605

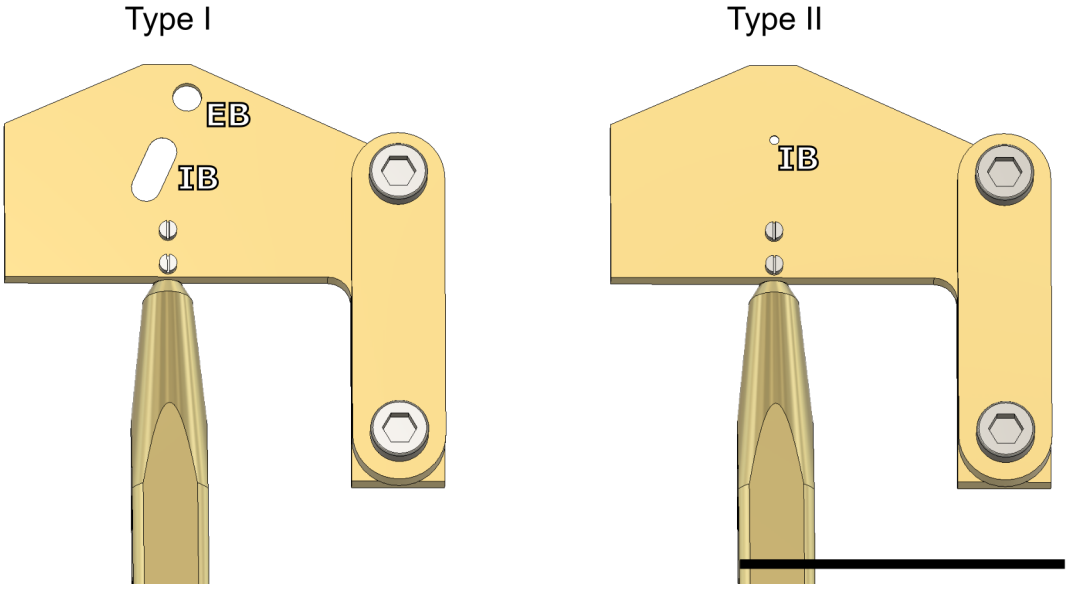

Supplementary Figure 1: Cryo-shutter designs. For Type I, an opening for the ion beam (IB) and the electron beam (EB) were considered. To reduce the contamination even further, the opening for the ion beam was minimized as much as possible in the cryo-shutter Type II. Moreover, the opening for the electrons was removed completely. With these modifications we could reduce contamination to a non-measurable level. Scale bar, 28 mm.

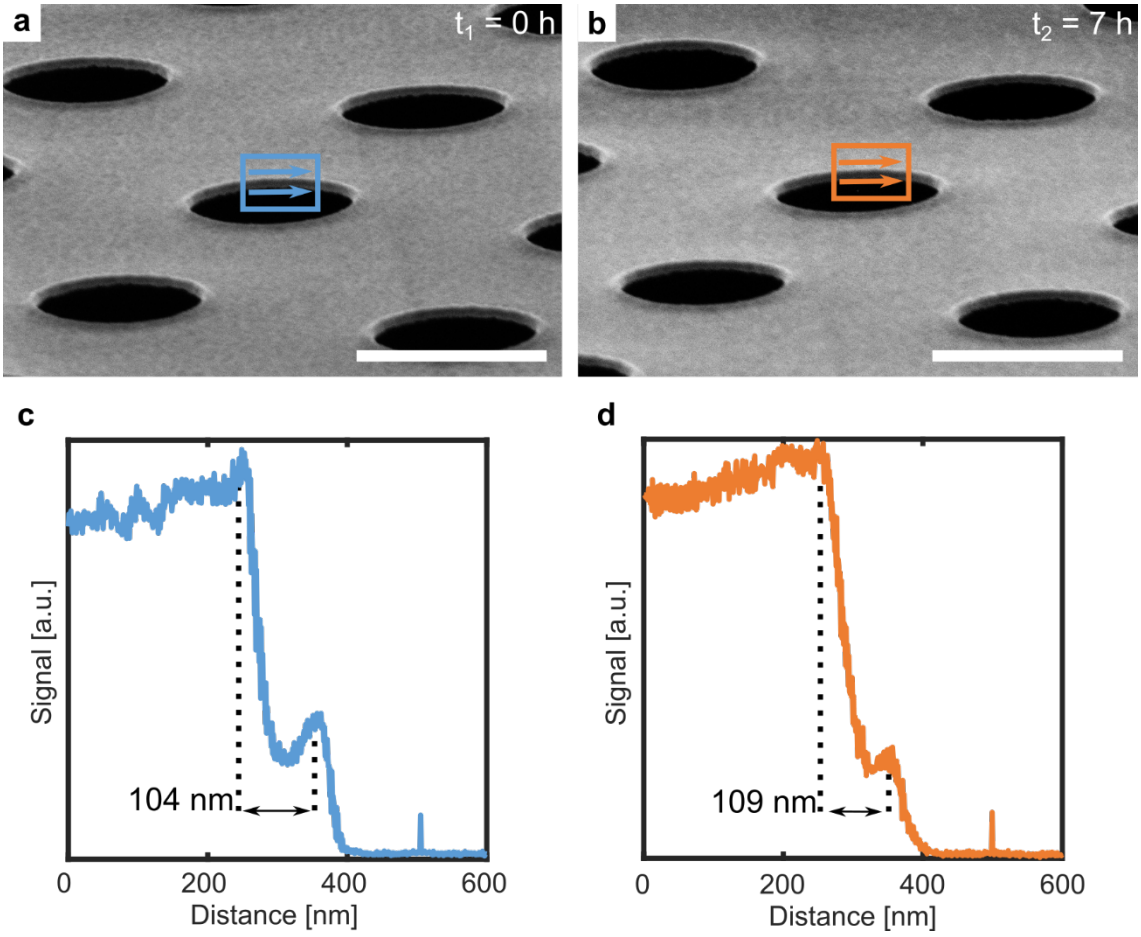

Supplementary Figure 2: Measurement of the amorphous ice contamination growth rate in the milling position. a) Before imaging, the stage, cryo-shield and the cryo-shutter were cooled. After reaching the final temperature of approximately -185°C, the stage was heated to -165°C. Since there might be a temperature offset of 15°C between stage and shuttle, we assume that the sample has a temperature of approximately -150°C. Whereas the cryo-shield reached a temperature of -185°C, the cryo-shutter could only be cooled to -177°C. To determine the amorphous ice contamination rate in the milling position, a holey gold EM grid (UltraAuFoil holey gold grid) was mounted to the cryo-FIB/SEM shuttle and loaded into the instrument. For the baseline measurements (t_1) the thickness of the holey gold film was determined (blue frame). To avoid ice ablation during focusing, beam tuning was done next to the region-of-interest. **b**) After 7 hours (t_2), another series of thickness measurement was performed on the same holes. **c**) Baseline measurements: Line profiles were averaged horizontally (blue arrows in a)). The upper and the lower edge of the profile (dotted black line) were fitted with Gaussian function. If fitting was not possible, edge positions were determined manually. The centers of the edges were used to calculate the thickness. **d**) Thickness determination after 7 h: The line profile was averaged and the thickness was determined as described in c). Finally, both values were corrected regarding the tilting angle of the grid and the total increase in thickness was determined. Herewith, the contamination rate can be calculated. Scale bars, 2 µm.

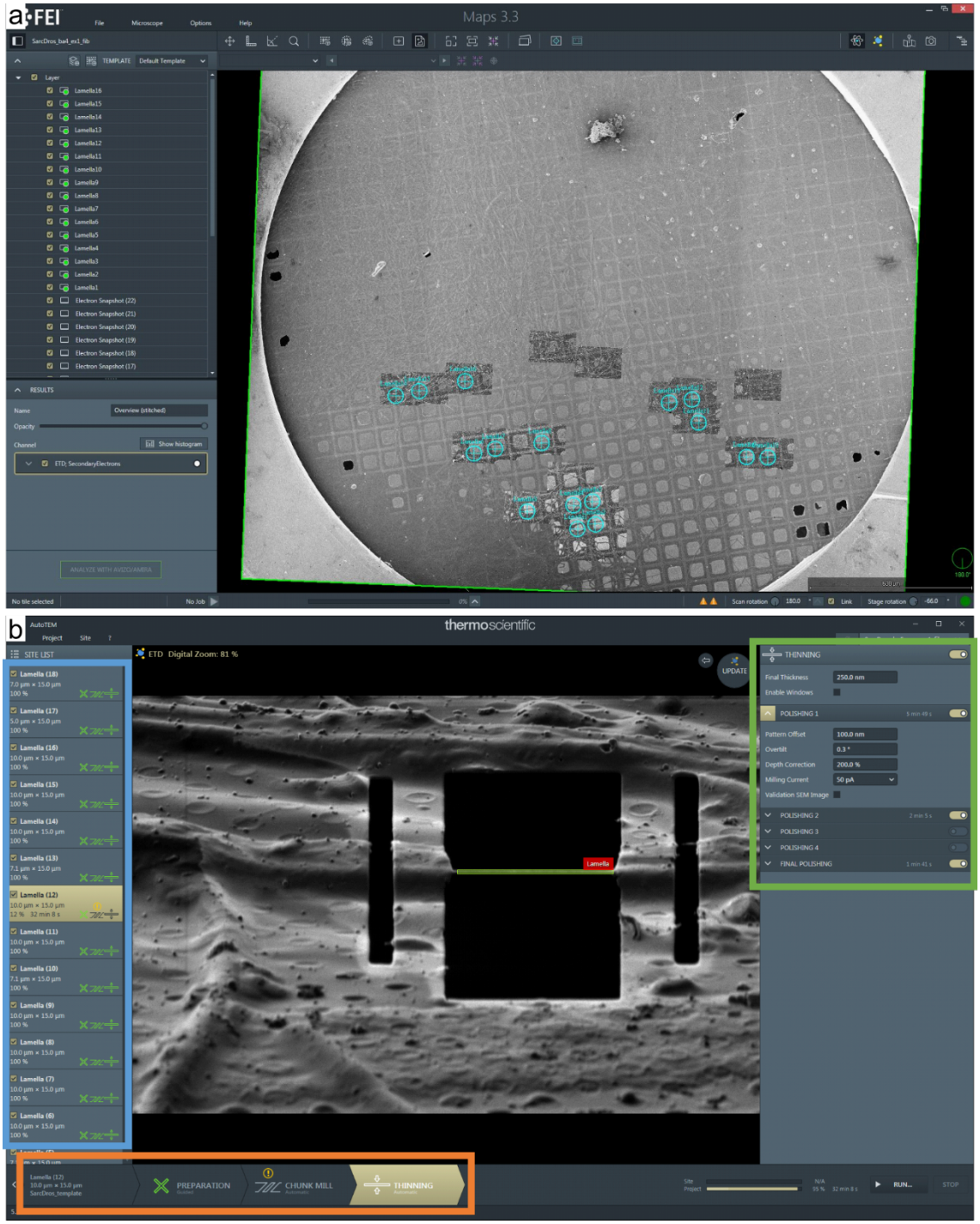

Supplementary Figure 3: Software applications. a) Overview of the MAPS software application. Either ROIs are identified by light cryo microscopy and uploaded in the MAPS software or identified directly in the overview image as shown here. **b**) Overview of the AutoTEM Cryo software application. The software pipeline is separated into three different tasks (orange frame): i) Site preparation, ii) rough milling iii) thinning. Each step consists of several sub-tasks (green frame) which can be tuned to guarantee an optimal performance for each lamella site (blue frame).

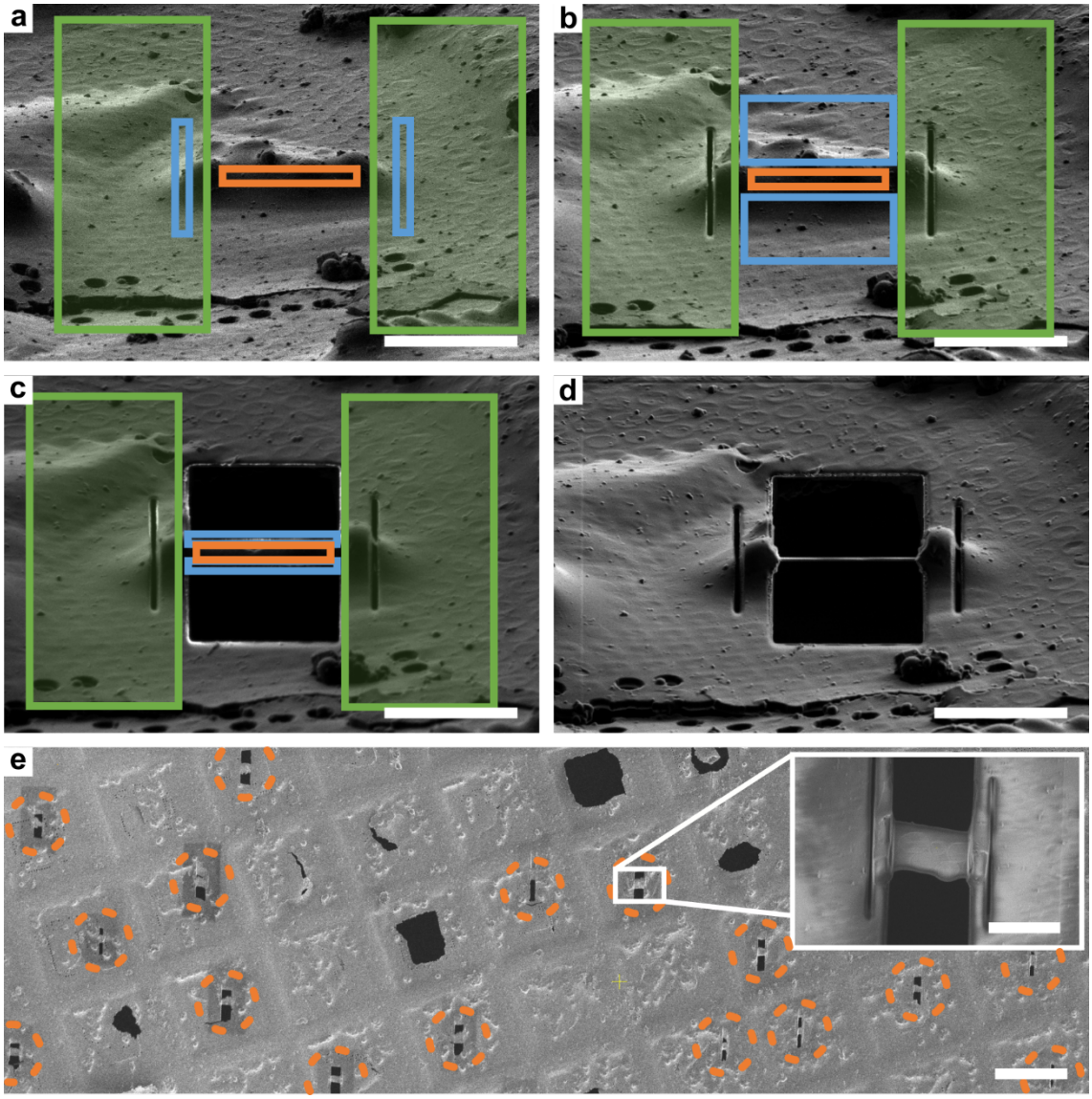

Supplementary Figure 4: AutoTEM pipeline for automated lamellae preparation. a) After the lamella site is centered, micro-expansion joints (blue frame) are milled next to the lamella site to release possible stress of the support layer. Scale bar, 10 µm. **b**) Thereafter, rough milling (blue frame) is performed in four consecutive steps. First, the bulk material is ablated with relatively high currents (0.5 – 1 nA). In the subsequent steps, the lamella is thinned to a thickness between 250 – 500 nm with an ion current of 0.5 to 0.1 nA. This step is performed for all milling sites, before the final step is executed. Scale bar, 10 µm. **c**) In the last step, the lamella is polished (blue frame) with low ion beam currents (30 – 50 pA). Scale bar, 10 µm. In order to correct for possible stage drifts, specific regions of the ROI (green frames in a), b) and c)) are imaged frequently and compared by a newly developed, cross-correlation based algorithm. **d**) The final lamella thickness is optimally about 100 to 200 nm. Scale bar, 10 µm. **e**) Overview of the different lamella sites, prepared during the same session (dashed orange circles). Scale bar, 50 µm (Inset scale bar: 10 µm).

Condition	Stage temperature [°C]	Shield temperature [°C]	Status shutter	Contamination rate [nm h^{-1}] (*n*)
1	-188	RT	Not inserted	85 ± 7 (15)
2	-188	-177	Not inserted	72 ± 4 (8)
3	-188	-177	Inserted	12.8 ± 1.6 (15)
4	-165	-177	Inserted	5.6 ± 1.0 (15)
5	-188	-177	Inserted	-0.6 ± 1.3 (15)
6	-165	-177	Inserted	0 ± 2 (45)

Supplementary Table 1: Influence of the different hardware components on the amorphous ice contamination rate inside the cryo-FIB/SEM. The number of holes, which were used for thickness determination (sample size), is given by the number *n*. For each condition (see also Supplementary Figure 1a), two to three positions, containing at least four holes, were selected. The uncertainty is estimated by the standard deviation of the different conditions.

Sample	Defocus [µm]	Tilting range [°]	Increments [°]	Pixel size [Å]	Total Dose [e^-/Å]
***E. coli* overview**	50	0	0	22.8	10
***E. coli* tomograms**	1.5-3.5	± 60 dose symmetric	3	1.79	120

Supplementary Table 2: Imaging conditions for the presented data. The imaging conditions for the tomograms used for sub-volume averaging (shown in Figure 5) and the TEM image (shown in Figure 5) are listed.